Nonequilibrium transport in mesoscopic multi-terminal SNS Josephson junctions

M. S. Crosser,[1,2] Jian Huang,[1,*] F. Pierre,[1,†] Pauli Virtanen,[3] Tero T. Heikkilä,[3] F. K. Wilhelm,[4] and Norman O. Birge[1,‡]

[1]*Department of Physics and Astronomy, Michigan State University, East Lansing, Michigan 48824-2320, USA*

[2]*Department of Physics, Linfield College, 900 SE Baker Street, McMinnville, Oregon 97128, USA*

[3]*Low Temperature Laboratory, Helsinki University of Technology, P.O. Box 5100, FIN-02015 TKK, Finland*

[4]*Department of Physics and Astronomy and Institute for Quantum Computing, University of Waterloo, Waterloo, Ontario, N2L 3G1, Canada*

(Received 21 August 2007; published 28 January 2008)

We report the results of several nonequilibrium experiments performed on superconducting/normal/superconducting (S/N/S) Josephson junctions containing either one or two extra terminals that connect to normal reservoirs. Currents injected into the junctions from the normal reservoirs induce changes in the electron energy distribution function, which can change the properties of the junction. A simple experiment performed on a three-terminal sample demonstrates that quasiparticle current and supercurrent can coexist in the normal region of the S/N/S junction. When larger voltages are applied to the normal reservoir, the sign of the current-phase relation of the junction can be reversed, creating a "π junction." We compare quantitatively the maximum critical currents obtained in four-terminal π junctions when the voltages on the normal reservoirs have the same or opposite sign with respect to the superconductors. We discuss the challenges involved in creating a "Zeeman" π junction with a parallel applied magnetic field and show in detail how the orbital effect suppresses the critical current. Finally, when normal current and supercurrent are simultaneously present in the junction, the distribution function develops a spatially inhomogeneous component that can be interpreted as an effective temperature gradient across the junction, with a sign that is controllable by the supercurrent. Taken as a whole, these experiments illustrate the richness and complexity of S/N/S Josephson junctions in nonequilibrium situations.

DOI: 10.1103/PhysRevB.77.014528 PACS number(s): 74.50.+r, 73.23.−b, 85.25.Am, 85.25.Cp

I. INTRODUCTION

When a superconducting metal (S) and a normal metal (N) are placed in contact with each other, the properties of both metals are modified near the S/N interface. This effect, called the superconducting proximity effect, was widely studied in the 1960's.[1] Our microscopic understanding of the proximity effect underwent dramatic progress in the 1960's as a result of new experiments performed on submicron length scales, coupled with theoretical ideas about phase-coherent transport from mesoscopic physics. It is now understood that the conventional proximity effect in S/N systems and the dc Josephson effect in S/N/S junctions arise from the combination of three ingredients: Andreev reflection of electrons into holes (and vice versa) at the S/N interface, quantum phase coherence of electrons and holes, and time-reversal symmetry in the normal metal. Our new understanding of the proximity effect in equilibrium situations and in linear response transport is demonstrated by a wealth of beautiful experiments[2] and is summarized in several theoretical reviews.[3,4]

In the past several years, research in S/N systems has increasingly focused on nonequilibrium phenomena. Understanding nonequilibrium situations is more difficult than understanding near-equilibrium situations, because the electron energy distribution function in nonequilibrium may be quite different from a Fermi-Dirac function. In such situations, the behavior of a specific sample may depend critically on the rates of electron-electron or electron-phonon scattering. A pioneering work in this area was the demonstration by Baselmans *et al.*[5] that the current-phase relation of a S/N/S Josephson junction can be reversed, producing a so-called "π junction." This effect is produced by applying a voltage that suitably modifies the form of the distribution function.

This paper presents results of several experiments performed on S/N/S Josephson junctions with extra leads connecting the N part of the devices to large normal reservoirs. Samples are made from polycrystalline thin films of aluminum (S) and silver (N) deposited by thermal evaporation. Electrical transport is in the diffusive limit—i.e., the electron mean free path is much shorter than all other relevant length scales in the problem, including the sample length and the phase coherence length. In these experiments, the two superconductors are usually at the same potential, referred to as ground. Different voltages are applied to the normal reservoirs, which in most cases cause the distribution function in the structures to deviate strongly from a Fermi-Dirac distribution.

Several of the experiments have been analyzed quantitatively within the framework of the Usadel equations,[4,6] which are appropriate for S/N samples in the diffusive limit. The equilibrium component of the Usadel equation is a diffusion equation describing pair correlations in N and S. The nonequilibrium, or Keldysh, component consists of two coupled Boltzmann equations for the spectral charge and energy currents. Incorporating inelastic scattering into the Keldysh equations involves inserting the appropriate collision integrals; but this procedure has so far been followed fully in only a few cases. Moreover, the effect of inelastic scattering on the equilibrium component of the Usadel equation or the proximity effect on the collision integrals have never been included self-consistently to our knowledge. More commonly, researchers analyzing nonequilibrium phe-

nomena solve either the Keldysh equation without collision integrals, or the standard Boltzmann equation with collision integrals but without superconducting correlations, depending on which aspect of the problem is more important. At the end of this paper we compare these approaches as applied to the last experiment discussed in the paper.

The paper is organized as follows: Sec. II describes the sample fabrication and measurement techniques. Section III describes a simple experiment, called the "dangling arm," involving a three-terminal S/N/S device with a single extra lead to a normal reservoir. The dangling arm experiment was first reported by Shaikhaidarov *et al.*[7] We include it here because it provides a clear demonstration of the superposition of quasiparticle current and supercurrent in a S/N/S junction, an essential result for the remainder of the paper. Section IV describes the π-junction experiment in three- and four-terminal devices. The four-terminal sample allows a direct comparison of the situations present in the three-terminal π junction[8] and the original four-terminal π junction of Baselmans *et al.*[5] Section V discusses the behavior of the critical supercurrent as a function of magnetic field applied parallel to the plane of the sample, and shows the difficulty involved in trying to achieve a π junction by Zeeman splitting of the conduction electrons.[9,10] The theoretical calculation relevant to this geometry is given in the appendix. Section VI discusses an experiment in which supercurrent and quasiparticle current are independently controlled in a three-terminal S/N/S junction, leading to an effective temperature gradient across the junction.[11] The local distribution function is measured by a tunnel probe near one of the S/N interfaces. The discussion provides information that was not included in our previous report on this experiment.[12] Together these experiments demonstrate the richness of phenomena present in S/N/S Josephson junctions under nonequilibrium conditions.

II. EXPERIMENTAL TECHNIQUES

A. Fabrication

All samples in this work were fabricated using *e*-beam lithography. A bilayer of resist was deposited onto an undoped Si wafer covered only with its native oxide layer. The bilayer was formed by first depositing a copolymer $P(MMA/MAA)$, followed by a second layer of $PMMA$. The bilayer was exposed by 35-keV electrons and then developed to make a mask for evaporation. With the resist bilayer, it is possible to fabricate undercuts in the mask, allowing angled evaporation techniques to be used.[13] Therefore, multiple layers of different metals (either 99.99% purity Al or 99.9999% purity Ag) were sequentially deposited without breaking vacuum.

These techniques were used to prepare the sample shown in Fig. 1. To create the tunnel probe (TP), 30 nm of Al was deposited while the sample was tilted 45°, creating an actual thickness of about 21 nm of Al on the surface. Next, a mixture of 90%Ar-10% O_2 gas was leaked into the vacuum chamber to a pressure of 60 Torr. After 4 min, the chamber was evacuated again, in preparation for the following depositions: For the silver wires; labeled R_1, R_2, and R_N; 30 nm of

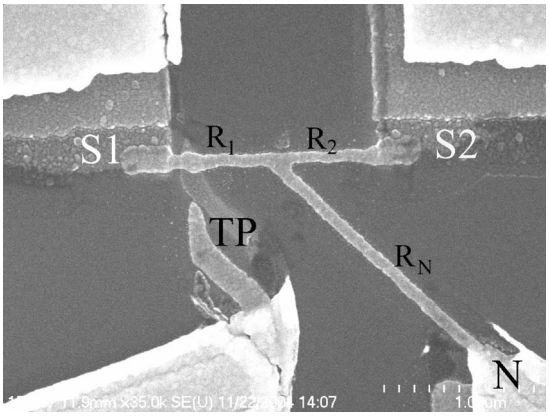

FIG. 1. SEM image of sample with two superconducting reservoirs, labeled S1 and S2, and normal reservoir labeled N. A tunnel probe, labeled TP, consists of thin Al oxidized prior to deposition of Ag wire.

Ag was deposited with the plane of the wafer perpendicular to the evaporation source. For the superconducting reservoirs S1 and S2, the sample was tilted 45° and rotated 180° in order to deposit 90 nm of Al (for a 60 nm thickness). Finally, the sample was rotated another 140 degrees in preparation for a final, thick layer of Ag to be deposited over the normal reservoir N. The sample in Fig. 6 followed a similar procedure, except foregoing the first Al deposition and oxidation steps.

B. Experimental setup

Samples were measured inside the mixing chamber of a top loading dilution refrigerator. All electrical leads to the sample passed through commercial LC π filters at the top of the cryostat and cold RC filters in the cryostat consisting of 2.2 kΩ resistors in series and 1 nF capacitors coupled to ground.

Current-voltage characteristics (I-V) curves) were obtained through four-probe measurements across the sample. The current was swept using a triangle wave and several cycles were collected and averaged together. Measurements of dI/dV were obtained by adding a slow ($\sim$1 mHz) triangle wave pattern to the sine output of a lock-in amplifier. The lock-in amplifier was operated at low frequencies (less than 100 Hz) to allow for extrapolation of the system response to zero frequency. Both the in-phase and out-of-phase components of the signal were recorded and utilized in the analysis.

III. DANGLING ARM EXPERIMENT

The dangling arm experiment was first proposed in the Ph.D. thesis of Gueron,[14] although a related geometry was discussed by Volkov two years earlier.[15] The experiment is performed on a three-terminal S/N/S Josephson junction sample similar to the one shown in Fig. 1, in which the tunnel probe in the lower left was unused. We label the three terminals of the sample S_1, S_2, and N, and the resistances of the three arms R_1, R_2, and R_N. (We neglect for the moment

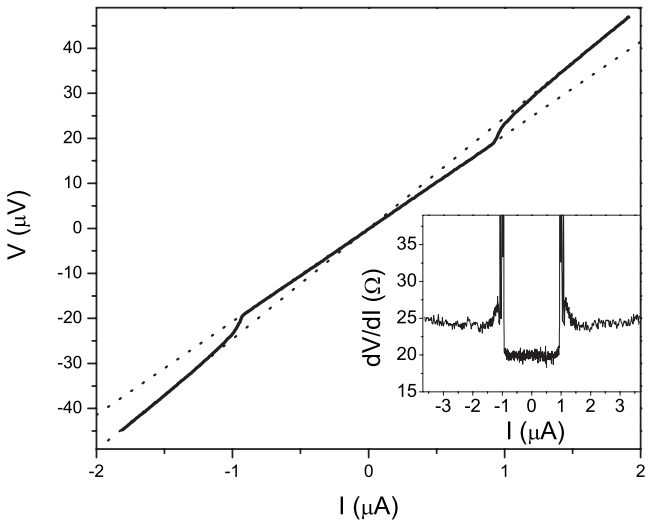

FIG. 2. Voltage versus current measured between reservoir N and S_1 with S_2 floating, at $T=51$ mK. Dotted lines represent slopes of 20.7 and 24.6 Ω, which correspond to the resistances R_P and R_N+R_1, respectively. Inset: Differential resistance vs current under similar conditions, showing agreement between the two measurement techniques.

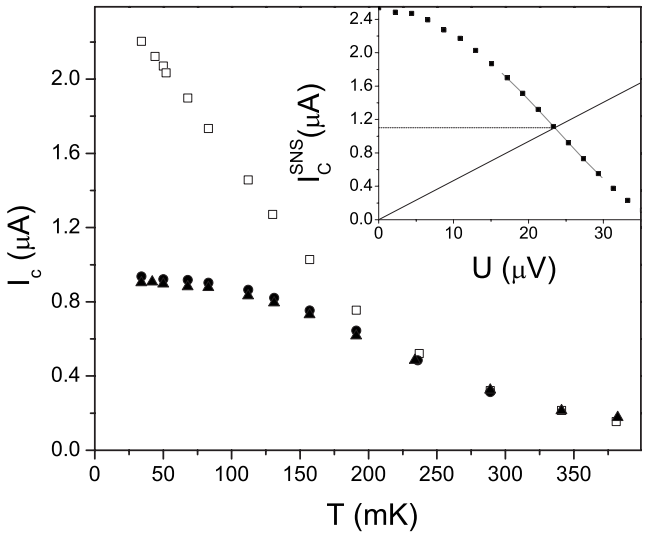

FIG. 3. Critical current measured between N and S_1 (●), between N and S_2 (▲), and between S_1 and S_2 (□)—the latter multiplied by the ratio $(R_1+R_2)/R_1 \approx 2$—for different temperatures. The three data sets are in close agreement at temperatures above about 250 mK. Inset: Graphical approach to calculation of low-temperature critical current between N and S_1. The dots are measurements of the critical current across S_1-S_2, again multiplied by $(R_1+R_2)/R_1$, as a function of applied voltage U between N and S_1. The critical current decreases rapidly with increasing U. The line through the origin represents the injected current from N. The intersection gives the critical current I_c^{NS} at the critical value of U. Note that all critical current values in the inset are 15–20 % larger than in the main panel, due to a small magnetic field $B=125$ G present when the latter data were obtained.

the variation of these resistances due to proximity effect.) One measures the resistance from N to S_1, while leaving S_2 open (dangling). Naively, one might expect the measured resistance between N and S_1 to be equal to R_N+R_1. That result would imply that the current travels directly from N to S_1, which in turn implies that S_1 and S_2 are at different voltages. Given that S_1 and S_2 are coupled by the Josephson effect, the relative phase ϕ between S_1 and S_2 then accumulates at the Josephson frequency $d\phi/dt=2eV_{12}/\hbar$. If, however, the injected current I splits into a piece I_1 through R_1 and a piece I_2 through R_2, such that $I_1R_1=I_2R_2$, then S_1 and S_2 will be at the same potential. To avoid having a net current flowing into the dangling arm, the sample must then provide a supercurrent I_S from S_2 to S_1 that exactly cancels the quasiparticle current I_2. In this scenario, R_1 and R_2 are effectively acting in parallel, and the measured resistance will be $R_P \equiv R_N+R_1R_2/(R_1+R_2)$.

Figure 2 shows the two-terminal I-V curve taken at $T=51$ mK from a sample similar to the one shown in Fig. 1, with nominal resistance values $R_1=7.0$ Ω, $R_2=7.0$ Ω, and $R_N=16.9$ Ω. The inset shows dV/dI vs I, providing a clearer view of the effective resistance. Either plot shows that the resistance is about 20.7 Ω when the applied current is less than about 0.94 μA. This resistance is very close to the nominal value of $R_P=20.4$ Ω. When the current exceeds 0.94 μA, the resistance increases to the value 24.6 Ω, which is very close to $R_N+R_1=23.9$ Ω. (Resistance differences less than an Ohm are attributed to the finite size of the T junction in the middle of the sample.) These data confirm the idea outlined in the previous paragraph, that supercurrent and quasiparticle current can coexist in the normal region of a S/N/S Josephson junction.

The transition at I_c^{NS} where the resistance increases to R_N+R_1 occurs when the supercurrent across the S/N/S Josephson junction exceeds the S/N/S critical current I_c^{SNS}. However, since only the fraction $I_2=IR_1/(R_1+R_2) \approx I/2$ of the injected current must be cancelled by the supercurrent, one should expect that $I_c^{NS}=I_c^{SNS}(R_1+R_2)/R_1$. The data in Fig. 3 show that this expectation is fulfilled at relatively high temperatures, but that at lower temperature I_c^{NS} falls well below this value.

Two reasons for the small values of I_c^{NS} at low temperature were given by Shaikhaidarov *et al.*[7] Those authors solved the Usadel equation analytically in the limit where the S/N interfaces have high resistance (poor transparency), so that proximity effects are small and the Usadel equation can be linearized. They pointed out that I_c^{SNS} is suppressed below its equilibrium value due to the applied voltage at N, a result we will reinforce below. They also argued that the phase-dependence of the resistances R_1, R_2, and R_N due to proximity effect causes the measured value of I_c^{NS} to be smaller than the nominal value $I_c^{NS}=I_c^{SNS}(R_1+R_2)/R_1$.

We believe that the effect related to the phase dependence of the resistances is small and the relative decrease in I_c^{NS} at low temperature is due predominantly to the decrease in I_c^{SNS} as a function of U. This effect is demonstrated graphically in the inset to Fig. 3. There the critical current of the Josephson junction I_c^{SNS} multiplied by the constant ratio $(R_1+R_2)/R_1$, is plotted as a function of the voltage U applied to the normal reservoir. As can be seen in the inset, I_c^{SNS} decreases rapidly as a function of U. The straight line through the origin in the

inset represents the current injected into the sample from the N reservoir U/R_P, where the resistances are evaluated at phase difference $\pi/2$ between S_1 and S_2. The intersection of the two curves shows the value of the dangling arm critical current I_c^{NS} (ordinate) at the critical voltage U_c^{NS} (abscissa). The figure demonstrates the large reduction in S/N/S critical current due to the applied voltage U, which explains why I_c^{NS} is much smaller than $I_c^{\mathrm{SNS}}(R_1+R_2)/R_1$ at low temperature. At high temperatures $T \gtrsim eU/k_B$, the relative reduction is less significant due to two reasons: First, increasing the temperature decreases the critical current I_c^{SNS}, and thereby also U_c^{NS}. Moreover, to observe a sizable reduction in $I_c^{\mathrm{SNS}}(U)$, $|eU|$ has to exceed k_BT.

IV. S/N/S NONEQUILIBRIUM π JUNCTION

A. Three-terminal π junction

Figure 3 shows, not surprisingly, that the critical current I_c of an S/N/S Josephson junction decreases when quasiparticle current is injected into the junction from a normal reservoir. Indeed, if the only effect of the injected current were to heat the electrons in the junction, then one would expect the critical current to continue decreasing monotonically as a function of the applied voltage U.[16] That this is not the case represents a major discovery in nonequilibrium superconductivity by Baselmans *et al.*[5] in 2000. Those authors showed that I_c first decreases as a function of U, but then increases again at higher U. The explanation[17,18] for this counterintuitive result consists of two pieces. First, one can view the supercurrent in the sample as arising from the continuous spectrum of Andreev bound states in the normal metal,[19,20] which carry supercurrent in either direction, depending on their energy. Second, in the presence of the applied voltage U the electron distribution function in the junction is not a hot Fermi-Dirac distribution, but is closer to a two-step distribution—as long as the short sample length does not allow electron thermalization within the sample.[21] The two-step distribution function preferentially populates the minority of Andreev bound states that carry supercurrent in the direction opposite to the majority, hence it reverses the current-phase relation in the junction.[17,18] Such a Josephson junction is called a "π junction" because the energy-phase and current-phase relations are shifted by π relative to those of standard Josephson junctions.

The original π-junction experiment of Baselmans *et al.* was performed in a four-terminal sample, where voltages of opposite sign were applied to the two normal reservoirs. Later, Huang *et al.*[8] demonstrated that a π junction can also be obtained in a three-terminal geometry with a single normal reservoir, a result predicted by van Wees *et al.*[22] 10 years earlier.

Figure 4(a) shows results of a three-terminal π-junction experiment performed on a sample similar to the one in Fig. 1, where the tunnel probe in the lower left portion of the figure is not used. We measure the I-V curve of the S/N/S Josephson junction using a four-probe current-bias measurement, while a dc voltage is simultaneously applied to the normal reservoir via a battery-powered floating circuit. Figure 4(a) shows a series of I-V curves at different values of

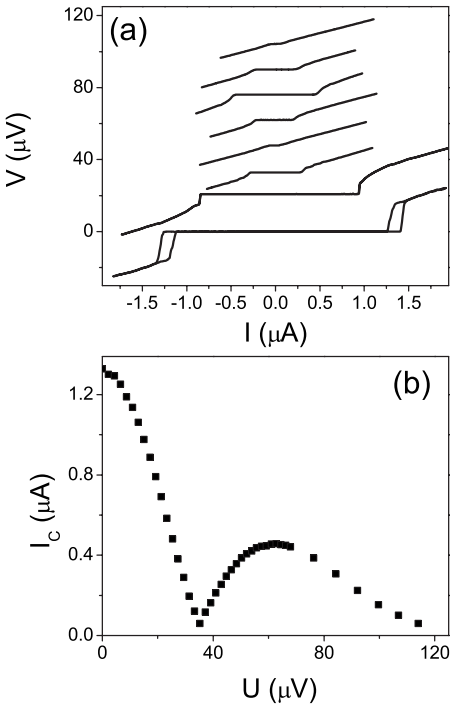

FIG. 4. (a) Voltage vs current across the S/N/S junction for selected voltages U applied to the normal reservoir. Graphs for different U are offset for clarity, with $U=0$, 17, 29, 35, 41, 63, 92, and 114 μV from bottom to top. The hysteresis in the $U=0$ data is probably due to heating of the Ag wire in the normal state. (b) Critical current vs U.

the voltage U applied to the normal reservoir. Figure 4(b) shows the critical current I_c vs U. Notice that I_c initially decreases with an increasing U, as shown in the inset to Fig. 3. But as U increases further, I_c reaches a minimum value (indistinguishable from zero in this experiment[23]) at $U=U_c \approx 34$ μV, then grows again to reach a second maximum at $U \approx 63$ μV. The minimum in I_c separates the standard Josephson junction behavior at low values of U from the π-junction behavior at higher U. If instead of plotting the critical current I_c (which is by definition a positive quantity) one were to plot the supercurrent I_s at a fixed phase difference $\phi=\pi/2$ across the junction then the graph would show a smooth curve passing through zero at $U=U_c$, reaching a local minimum at $U \approx 63$ μV and gradually returning to zero at large U.

B. Comparison of four-terminal π junctions with symmetric and antisymmetric bias

The physical explanation of the π junction in the three-terminal sample is the same as in the four-terminal sample, with the differences arising only from the distribution functions. Figure 5 shows a schematic drawing of the distribution function $f(E)$ along a path from a reservoir N to S for both four-terminal and three-terminal samples for $U \gg k_BT$, assuming weak electron-electron interactions in the N wire, and neglecting the proximity corrections. Notice in figures (c) and (d) that $f(E)$ consists of a double-step function, the

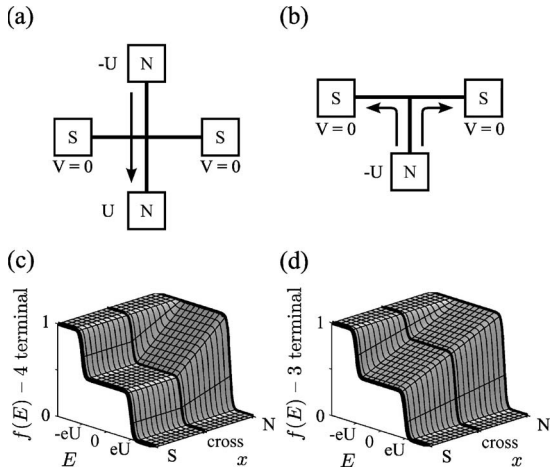

FIG. 5. (a) Depiction of electron flow in the four-terminal configuration. (b) Depiction of electron flow in three-terminal configuration. (c) Schematic representation of the distribution function on the path between a normal (N) and superconducting (S) terminal in the structure (a) under high bias $U \gg k_B T$. (d) Distribution function in the T structure (b) under similar conditions. Due to Andreev reflection $f(\varepsilon)$ is discontinuous at the N-S interface as explained in the text.

step height within the energy range $-eU$ to eU changing with the location along the wire. As we will show in the next section, the even (in energy) part of $f(E)$ has no effect on the magnitude of the supercurrent (in the absence of electron-electron interactions), suggesting that the voltage-dependent critical current $I_c(U)$ would be identical in three-terminal and four-terminal samples with identical dimensions and resistances. However, there are three reasons why this is not quite true: First, Joule heating is more prevalent in the four-terminal device, which rounds the distribution functions more than in the three-terminal device. Second, the spectral supercurrent density $j_E(E)$, evaluated at the junction point will be slightly smaller in the four-terminal sample than in the three-terminal sample due to the presence of the additional arm connecting the sample to a normal reservoir.[20] Finally, $f(E)$ will be slightly more rounded in the four-terminal sample due to the increased phase space available for electron-electron interactions. Roughly speaking, the rate of *e-e* interactions at a given energy is proportional to $f(E) \times [1-f(E)]$, which is maximized when $f(E)=1/2$. Each of these effects serve to increase I_c in the three-terminal geometry relative to the four-terminal geometry.

It is not practical to compare critical currents from two different samples, since they will never have identical dimensions nor electrical resistances. Instead, it was proposed in Ref. 8 to compare the critical currents in a single four-terminal sample under conditions of symmetric and antisymmetric voltage bias of the two normal reservoirs. Figure 6 shows the sample we fabricated for this experiment, with the superconductive reservoirs labeled S1 and S2 and the normal reservoirs labeled N1 and N2. By applying a positive potential U to N1 and a negative potential $-U$ to N2, one reproduces the experiment performed by Baselmans *et al.* We call this situation antisymmetric bias, since the two applied voltages differ by a negative sign. In this case the quasiparticle current overlaps with the supercurrent only at the crossing point of the sample where the electrostatic potential is equal to zero. In contrast, applying the identical voltage U on both N1 and N2 (with ground defined at one of the superconducting electrodes), called symmetric bias, will produce a situation mimicking that in the three-terminal experiment of Huang *et al.*[8] Notice that by mimicking a three-terminal sample with a four-terminal sample, geometrical differences between the two experiments are eliminated, so any observed difference in the critical currents will be due either to *e-e* interactions or to Joule heating.

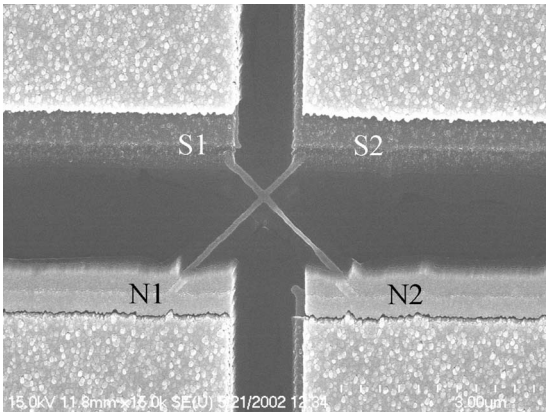

FIG. 6. SEM image of S/N/S Josephson junction. The X shape is deposited Ag that connects to (difficult to see) Al reservoirs above and Ag reservoirs below patterned by angled evaporation. The feature in the Ag wire near N2 is likely due to a near burn in the sample.

The preceding description of symmetric and antisymmetric biases holds strictly only if the resistances of the two lower arms are identical. Otherwise, application of antisymmetric bias will result in a nonzero potential at the cross and some quasiparticle current will flow into the superconducting reservoirs. In that case, $f(E)$ will take a form intermediate between those depicted in Figs. 5(c) and 5(d), which decreases the measurement contrast between the two biases. In our experiments we took care to measure the resistances of all the arms and to ensure that the voltages at the two normal reservoirs were indeed equal (for symmetric bias) or opposite (for antisymmetric bias).

Figures 7(a) and 7(b) show *I-V* curves measured across the S/N/S junction at $T=170$ mK, for several different values of U. Curves with increasing values of U are offset upward for clarity. Figure 7(a) shows the data for antisymmetric bias while Fig. 7(b) shows symmetric bias. The data follow the same trend observed in Fig. 4, namely, the critical current first decreases with increasing U, then increases again before finally disappearing altogether. Figure 8(b) shows this critical supercurrent as a function of U. In this figure we have plotted the critical current as negative in the range of voltages after I_c disappears initially, to signify that the junction is in the π state as discussed earlier.

The transition from the 0 state to the π state can be confirmed directly by experiment,[5] without recourse to the theoretical explanation. The resistances of the Ag arms of the

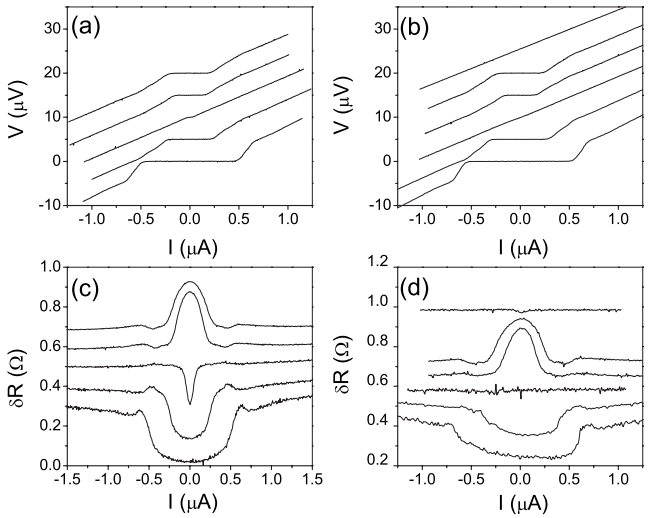

FIG. 7. Data showing voltage drops across segments of wire either in antisymmetric or symmetric arrangements while current flows from S1 to S2. Each line (offset for clarity) corresponds to a different value of U. (a) Voltage across S1 to S2 for the antisymmetric measurement. Applied voltages U are from the bottom: 19, 28, 38, 52, and 71 μV. (b) Voltage across S1 to S2 for the symmetric measurement. Applied U: 17, 25, 37, 49, 72, and 131 μV. (c) Resistance across N1 to N2 for the antisymmetric measurements. (d) Resistance across N2 to S2 for the symmetric measurements, taken from voltage measurements in which a constant resistance was subtracted from the graph.

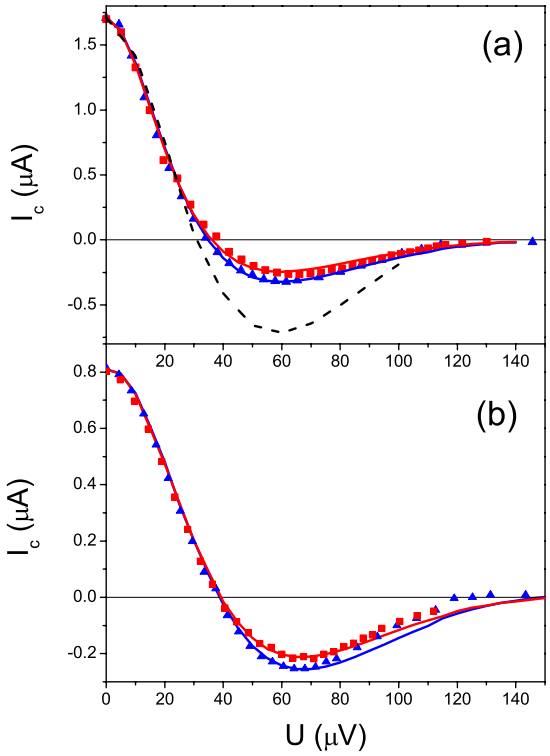

FIG. 8. (Color online) Critical current of a four-terminal S/N/S Josephson junction versus voltage U applied to the normal reservoirs. The voltages are applied either antisymmetrically (■) or symmetrically (▲) to the two reservoirs. Solid lines represent simultaneous best fits to data at different temperatures. Fitting methods are discussed in the text for data taken at bath temperatures (a) 35 mK and (b) 170 mK. The dashed line represents the best fit when Joule heating is excluded.

sample vary with the phase ϕ due to the proximity effect.[24] The phase ϕ, in turn, varies between $\pm\pi/2$ as a function of the supercurrent I_S passing between S_1 and S_2; hence, one observes a variation of the resistances as a function of I_S. This effect is shown in Figs. 7(c) and 7(d), in which the resistances between N_1 and N_2 (N_1 and S_2) were measured versus I_S for the antisymmetric and symmetric bias configurations, respectively. Each curve in the lower two figures has the same value of U as the corresponding I-V curve in the upper figures. One can see that proximity effect induces a local minimum in the resistance at $I_s=0$ when the junction is in the 0 state, because that is where $\phi=0$. In contrast, the resistance exhibits a local maximum in the resistance at $I_s=0$ when the junction is in the π state, because $\phi=\pi$. Interestingly, the top curve in Fig. 7(d) shows that at large enough values of U, the system returns to the 0 state since the resistance again shows a local minimum at $I_s=0$. This high-U transition from the π state back to the 0 state was not visible in the S/N/S I-V curves.

Figure 8 shows the behavior I_c vs U at two different temperatures. The squares represent antisymmetric bias while triangles represent symmetric bias. Both bias configurations appear similar in that the samples cross to the π state at nearly the same value of U. It should be noted, however, that the maximum π current is larger for symmetric bias than for antisymmetric bias. That result is consistent with the qualitative arguments made above. In the next section we present a quantitative analysis of the results.

C. Calculation of the critical current in an S/N/S Josephson junction

The amount of supercurrent passing through an S/N/S Josephson junction may be calculated by[17]

$$I_S = \frac{\sigma_N A}{2}\int_{-\infty}^{\infty} dE[1-2f(E)]j_E(E) \tag{1a}$$

$$= \sigma_N A \int_0^{\infty} dE f_L(E) j_E(E), \tag{1b}$$

where σ_N and A are the conductivity and cross-sectional area of the normal metal, respectively. $f(E)$ is the distribution function within the normal wire and $f_L(E) \equiv f(-E) - f(E)$ is the antisymmetric component of $f(E)$ with respect to the potential of the superconductors. The spectral supercurrent density $j_E(E)$ is an odd function of energy, and describes the amount of supercurrent at a given energy traveling between superconductors with relative phase difference ϕ. In the samples considered in the present work, it is generally sufficient to calculate the supercurrent using the the distribution function at the crossing point of the wires.

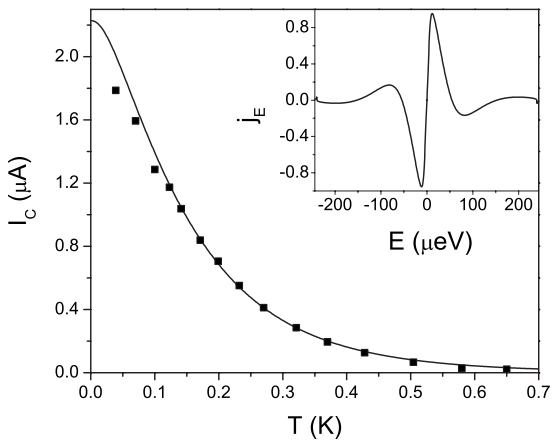

FIG. 9. Critical current I_c at several temperatures for the sample shown in Fig. 6. The line is the best fit by solving equation (1b) with a Fermi-Dirac distribution function. Inset: Solution for spectral supercurrent used to fit data.

To determine $j_E(E)$, we solve the Usadel equation numerically using the known physical dimensions and electrical resistances of the various wire segments of the sample. We then look for consistency with the measured temperature dependence of the equilibrium critical current $I_c(T)$ shown in Fig. 9. The $j_E(E)$ used to fit these data, evaluated at $\phi = \pi/2$, is shown in the inset of Fig. 9. Since the length L of the junction is much longer than the superconducting coherence length ξ_s of the S electrodes for all the samples studied in this work, the damped oscillations in $j_E(E)$ occur on an energy scale given by the Thouless energy $E_{\mathrm{Th}}=\hbar D/L^2$, where D is the diffusion constant in the wire. E_{Th} characterizes the temperature scale over which the equilibrium critical current drops to zero, and also determines the voltage scale U needed to create a nonequilibrium π junction. The transition from the 0 state to the π state occurs at $eU \approx 8E_{\mathrm{Th}}$. The fit shown in Fig. 9 was obtained with $E_{\mathrm{Th}}=4.11$ μeV.

Next we calculate $f(E)$ in the nonequilibrium situation with antisymmetric bias, i.e., with voltages U and $-U$ applied to reservoirs N_1 and N_2. Because we are interested in the distribution function far from the superconducting reservoirs, we consider $f(E)$ using the Boltzmann equation. Let us first ignore the supercurrent and proximity effects, although inclusion of those effects will be discussed in detail in Sec. VI. In a reservoir at voltage U, $f(E)$ is a Fermi-Dirac distribution displaced by energy eU, $f(E)=f_{\mathrm{FD}}(E-eU)=\{\exp[(E-eU)/k_BT]+1\}^{-1}$. In the experiment with antisymmetric bias, we then have $f(E)=f_{\mathrm{FD}}(E-eU)$ at reservoir N_1 and $f(E)=f_{\mathrm{FD}}(E+eU)$ at reservoir N_2. If we neglect inelastic electron scattering, then in the middle of the wire (at the intersection of the cross) $f(E)$ has the double-step shape

$$f(E) = \frac{1}{2}[f_{\mathrm{FD}}(E+eU) + f_{\mathrm{FD}}(E-eU)]. \tag{2}$$

In fact, the odd part of $f(E)$ is the same everywhere in the Ag wire

$$f_L(E) = \frac{1}{2}\left[\tanh\left(\frac{E-eU}{2k_BT}\right) + \tanh\left(\frac{E+eU}{2k_BT}\right)\right]. \tag{3}$$

This conclusion holds also in the presence of the proximity effect. At energies $|E|<eU$, the even part $f_T(E)$ varies linearly with distance between the two reservoirs (the lower two arms of the sample), but is zero everywhere along the direct path connecting the two superconductors (in the ideal case where the resistances of the two lower arms are equal).

To calculate $f(E)$ in the experiment with symmetric bias, we need the boundary conditions at the interfaces between the normal wires and the superconducting reservoirs. For energies below the superconducting gap Δ these conditions are $f_T=0$ and $\partial f_L/\partial x=0$, where $f_T(E)\equiv 1-f(E)-f(-E)$. These boundary conditions assume high-transparency interfaces, no charge imbalance in the superconductors, and no heat transport into the superconductors.[25] [Note that $f_L(E)$ is discontinuous at the N-S interface for energies below the gap, and returns to the standard form $\tanh(E/2k_BT)$ in the S electrodes.] The solution for $f(E)$ at the N/S interface is identical to Eq. (2), but the symmetric component $f_T(E)$ is nonzero elsewhere in the wire. Notice that the odd component of the distribution function $f_L(E)$ is identical in the two cases everywhere in the sample. The proximity effect induces a small feature in $f_L(E)$ discussed in Sec. VI, but it is zero at the crossing point in the middle of the sample.

Calculation of $f(E)$ in the realistic situation requires consideration of electron-electron interactions in the Ag wire. (The electron-phonon interaction, in contrast, is much weaker, and need be considered only in the massive normal reservoirs. See the discussion below.) To incorporate electron-electron interactions, we solved the Boltzmann equation in the wire numerically, following previous work by Pierre.[26,27] The results of this numerical calculation of $f(E)$ in the situations with either symmetric or antisymmetric bias were extremely similar. Indeed, the slight additional rounding of $f(E)$ in the antisymmetric case could not account for the differences observed in the experiment, shown in Fig. 8.

To account for the difference in the observed $I_c(U)$ between the two experiments, we next considered the effect of Joule heating on the temperatures of the normal reservoirs. (Due to Andreev reflection at the N/S interfaces, there is no heat transport into the superconducting reservoirs.) Although we intentionally fabricated the normal reservoirs much thicker than the wires, this was not enough to eliminate the effects of Joule heating altogether. The heat current in a reservoir at a distance r from the juncture with the wire is given by

$$\vec{j}^{Q} = -\pounds\sigma T\nabla T \equiv \frac{P}{\theta r t}\hat{r}, \tag{4}$$

where $P=I^2R$ is the total power dissipated in the wire, σ and $t=310$ nm are the conductivity and the thickness of the reservoir, respectively, and $\pounds \equiv \pi^2/3(k_B/e)^2 = 2.44 \times 10^{-8}$ V^2/K^2 is the Lorenz number. (We neglect the small additional Joule heat generated in the reservoirs themselves.) The spreading angle $\theta \approx \pi$ if we consider the combination of the two normal reservoirs shown in Fig. 6.

Using Eq. (4) as a boundary condition, one can find an effective temperature at the wire-reservoir interface equal to[28]

$$T_{\text{eff}} = \sqrt{T^2 + b^2 U^2}. \tag{5}$$

The temperature far away in the normal reservoir is assumed to be T, the bath temperature. The factor b is given by[29]

$$b^2 = \frac{R_\square}{\theta \pounds R} \ln \frac{r_1}{r_0}, \tag{6}$$

where $R_\square \equiv 1/(\sigma t)$ is the sheet resistance of the normal reservoir, $r_0 \approx$ the wire width, and r_1 is the distance over which the electrons in the reservoir thermalize to the bath temperature via electron-phonon scattering. The parameter b varies inversely with the thickness of the metal reservoir and the electrical resistance encountered by the quasiparticle current in the wire. Because the voltage drop U in the antisymmetric bias situation occurs entirely between a normal reservoir and the crossing point, the resistance R is smaller than in the symmetric bias situation where U drops fully from the N reservoirs to the N/S interfaces. The larger current in the former case causes more Joule heating, and hence a larger reservoir temperature. For our sample, the values of b needed to fit the data [see solid lines in Figs. 8(a) and 8(b)] are 2.7 and 3.2 K/mV, respectively, for the symmetric and antisymmetric bias experiments. Their ratio of 1.2 matches the ratio calculated from the sample parameters. Their magnitudes, however, are nearly three times larger than what we calculate based on the total reservoir thickness. The experiment seems to suggest that heat was trapped in the 35-nm Al layer at the bottom of the reservoirs, rather than immediately spreading throughout the whole reservoir thickness.[30]

V. APPLICATION OF A PARALLEL MAGNETIC FIELD AND THE "ZEEMAN" π JUNCTION

There is a long history of applying magnetic fields perpendicular to the direction of current flow in superconductor/insulator/superconductor (S/I/S) Josephson junctions, to observe the famous Fraunhofer pattern in the critical current. In S/N/S junctions, the Fraunhofer pattern is observed only in wide junctions, whereas narrow junctions exhibit a monotonic decrease of the critical current with field due to the orbital pair-breaking effect.[31]

In this section we discuss the effect of a magnetic field applied parallel, rather than perpendicular, to the current direction. In this geometry there should never be a Fraunhofer pattern. And because the samples are thin films, one expects the orbital pair-breaking effect to be much weaker than for a field applied perpendicular to the plane. In the case of an extremely thin sample the Zeeman (spin) effect should dominate over the orbital effect of the field.

The effect of Zeeman splitting on an S/N/S Josephson junction was studied theoretically in 2000 by Yip[10] and by Heikkilä *et al.*[9] Their idea is that the electronic structure of a normal metal in a large applied magnetic field resembles that of a weak ferromagnet, in that the up and down spin bands are displaced by the Zeeman energy. They also showed how

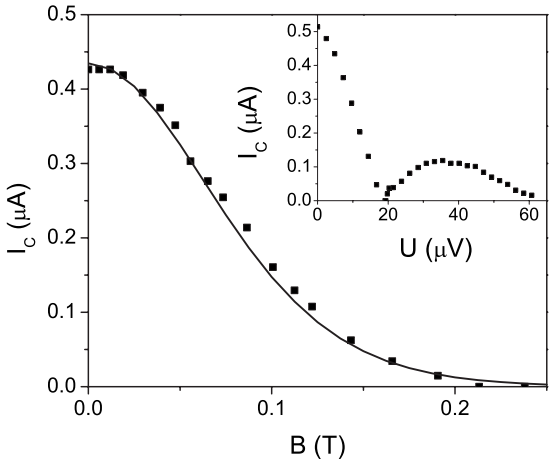

FIG. 10. Critical current across S/N/S junction as a function of external magnetic field applied parallel to the current direction. In the absence of orbital pair-breaking effects, the transition into the π state would be expected near 0.35 T. Markers indicate experimental results and solid line the scaling (7) obtained from the Usadel equation. Inset: Critical current versus applied voltage for same sample, showing transition to the π state at $U=20$ μV.

the Zeeman-split junction behaves analogously to the nonequilibrium S/N/S junction, with the Zeeman energy playing the role of the voltage in Eqs. (1b) and (3). Josephson junctions made with real ferromagnetic materials (S/F/S junctions) are the subject of intense current interest, as they can also show π-junction behavior.[32] Unlike the π-junctions discussed earlier in this paper, however, the π junctions in S/F/S systems occur in equilibrium. They appear only in particular ranges of the F-layer thickness, due to spatial oscillations in the superconducting pair correlations induced in the F metal near the F-S interface by proximity effect. Those oscillations, in turn, arise from the different Fermi wave vectors of the spin-up and spin-down electrons in the F metal. In diffusive S/F/S junctions, the sign of the coupling between the two superconductors oscillates over a distance scale $\xi_F = (\hbar D/E_{\text{ex}})^{1/2}$, where D is the diffusion constant and E_{ex} is the exchange energy in the ferromagnet. In the standard elemental ferromagnets, E_{ex} is large ($\approx$0.1 meV), hence ξ_F is extremely short—on the order of 1 nm. Control of sample thickness uniformity at this scale is difficult, hence several groups have used dilute ferromagnetic alloys, with reduced values of E_{ex}, to increase ξ_F. The advantage of the "Zeeman" π junction is that it is fully tunable by the field. The disadvantage is that the sample must be thin enough to minimize the effects of orbital pair breaking in both the superconducting electrodes and in the normal part of the junction.

Figure 10 shows a plot of I_c vs B in an S/N/S sample whose normal part had length $L=1.4$ μm, width $w=50$ nm and thickness $t=33$ nm. The critical current decreases monotonically to zero, over a field scale of $\approx$0.1 T. This result might appear surprising at first glance: At a field $B=0.1$ T, the magnetic flux enclosed in the cross section of the wire perpendicular to the field is only $\Phi \approx 1.6 \times 10^{-16}$ T m^2 $=0.08\Phi_0$, where $\Phi_0 = h/2e$ is the superconducting flux quantum. Furthermore, separate tests of the Al banks confirm that

they remain superconducting to fields of order 0.85 T.

A quantitative understanding of the data in Fig. 10 can be obtained from a solution to the Usadel equation. The analysis discussed in the Appendix shows how a parallel magnetic field can be absorbed into a spin-flip rate Γ_{sf} in the equations. This allows us to apply the scaling $I_c(B)/I_c(B=0) \approx \exp(-0.145\Gamma_{sf}/E_{Th})$ for the zero-temperature supercurrent of an S/N/S junction found in Ref. 33 and find

$$I_c(B)/I_c(B=0) \approx e^{-(B/B_1)^2}, \tag{7}$$

$$B_1 \approx 6.43\frac{\hbar\sqrt{w^2+t^2}}{eLwt} \approx 0.10 \text{ T}. \tag{8}$$

Our numerical calculations confirm that this scaling also applies in our multiprobe experimental geometry. This prediction is in a good agreement with the experiment, as seen in Fig. 10.

In the limit $w \gg t$, the characteristic field scale B_1 varies as Φ_0/Lt, rather than the more intuitive result Φ_0/wt we might expect based on the cross-sectional area of the wire perpendicular to the field. The physical explanation for this result was given by Scheer *et al.*[34] in a paper discussing universal conductance fluctuations as a function of parallel field in normal metal wires. As an electron travels down the length of a long diffusive wire, its trajectory circles the cross section of the wire many times—on the order of $N \approx (L/w)^2$. Because diffusive motion can be either clockwise or counterclockwise as seen looking down the wire, the standard deviation in net flux and accumulated phase between different trajectories is approximately proportional to $Bwt\sqrt{N} = BLt$, which gives the scaling for dephasing.

It is instructive to ask what constraints on the sample geometry would have to be met to enable observation of the Zeeman π junction. We estimate the Thouless energy of the sample discussed in Fig. 10 to be $E_{Th} \approx 2.5$ μeV both from the temperature dependence of I_c (not shown), and from the voltage-induced transition to the π state at $U_c = 20$ μV (inset to Fig. 10). According to theory, the Zeeman π junction should occur when $g\mu_B B \approx 16E_{Th}$,[9,10] or $B = 0.35$ T. Attempts to make thinner samples in order to increase the field scale B_1 in Eq. (7) were unsuccessful, due to the tendency of very thin Ag films to ball up. According to the theory, much thinner films, with t/L of the order of $0.2g\mu_B/eD \sim 0.001$, will be required to enable observation of the Zeeman π junction.

VI. ENGINEERING THE DISTRIBUTION FUNCTION

The discussion in Sec. IV B implied that the three-terminal and four-terminal π junctions are similar, with only minor differences due to a slight decrease in the phase space available for electron-electron interactions in the three-terminal case. But that oversimplified discussion misses some important physics. Heikkilä *et al.*[11] showed that the superposition of quasiparticle current and supercurrent in the horizontal wire in the three-terminal sample induces a change $\delta f(E)$ in the distribution function at energies of order E_{Th}. The new feature is antisymmetric in space and energy (see Fig. 16 for the theoretical prediction and our experimental results which follow each other nicely), and can be interpreted as a gradient in the effective electron temperature across the S/N/S junction. For this reason, the result was dubbed a "Peltier-like effect." Although a tiny cooling effect does occur, observing it in a real electron temperature would require a slightly modified experimental setup.[35] In the present case, one should view this effect mostly as a redistribution of the Joule heat generated in the sample by the applied bias U.

In Sec. IV C it was discussed how the distribution functions behave in the absence of proximity effects and supercurrent. Including these effects, but ignoring inelastic scattering, results in the kinetic equations[36]

$$\frac{\partial j_T}{\partial x} = 0, \quad j_T \equiv D_T(x)\frac{\partial f_T}{\partial x} + j_E f_L + T(x)\frac{\partial f_L}{\partial x}, \tag{9a}$$

$$\frac{\partial j_L}{\partial x} = 0, \quad j_L \equiv D_L(x)\frac{\partial f_L}{\partial x} + j_E f_T - T(x)\frac{\partial f_T}{\partial x}, \tag{9b}$$

where $j_T(E)$ and $j_L(E)$ are the spectral charge and energy currents, respectively. The energy-dependent coefficients D_T, D_L, j_E, and T can be calculated from the Usadel equation,[6,36] and vary with the superconducting phase difference ϕ between S_1 and S_2. In general, these equations must be solved numerically; however, they can be solved analytically by ignoring the energy dependence in D_T and D_L and neglecting the T terms. One can show that, in the presence of both the applied voltage U and a nonzero supercurrent between S_1 and S_2, f_L along the horizontal wire connecting the two superconductors contains a spatially antisymmetric contribution proportional to $j_E(E)$. In the exact numerical solution to Eqs. (9), the feature is distorted due to the rapid evolution of the diffusion coefficients D_T and D_L near the N/S interfaces.[11]

The antisymmetric feature in $f(E)$ can be measured by performing tunneling spectroscopy with a local superconducting tunnel probe, which has been demonstrated by Pothier *et al.*[21] to reveal detailed information about $f(E)$ in a metal under nonequilibrium conditions. In our case, the local probe must be placed close to the N/S interface where the predicted feature in $f(E)$ has its maximum amplitude. This location introduces a new difficulty in our experiment because the density of states (DOS) of the Ag wire near the N/S interface is strongly modified by proximity effect. Hence we must first determine the modified DOS at equilibrium before we measure $f(E)$ under nonequilibrium conditions.

The current-voltage characteristic of the probe tunnel junction is

$$I(V) = -\frac{1}{eR_T}\int dE n_{Al}(E)\int d\varepsilon P(\varepsilon) \times \{f_{Al}(E)n_{Ag}(E-eV-\varepsilon)[1-f_{Ag}(E-eV-\varepsilon)] - [1-f_{Al}(E)]n_{Ag}(E-eV+\varepsilon)f_{Ag}(E-eV+\varepsilon)\}, \tag{10}$$

where R_T is the normal state tunnel resistance, n_{Ag} and n_{Al} are the normalized densities of states, and f_{Ag} and f_{Al} are the

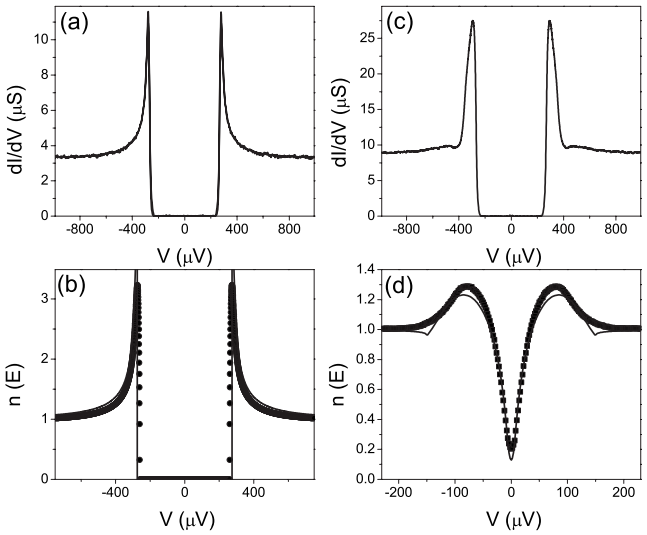

FIG. 11. (a) Differential conductance data and their best fit for the reference S/I/N tunnel junction at $B=13$ mT and $T=40$ mK. (b) Circles are the Al density of states $n_{\mathrm{Al}}(E)$ used to produce the fit in part (a). (The solid line shows the ideal BCS DOS without a magnetic field, for comparison.) (c) The dI/dV data and their best fit in equilibrium for the tunnel probe on the sample shown in Fig. 1, at $B=12.5$ mT. (d) Squares are the $n_{\mathrm{Ag}}(E)$ used to produce the fit in part (c). The solid line is a fit to the solution of the Usadel equation discussed in the text.

electron energy distribution functions on the Ag and Al sides of the tunnel junction, respectively. The function $P(\varepsilon)$ characterizes the probability for an electron to lose energy ε to the resistive environment while tunneling across the oxide barrier, an effect known as "dynamical Coulomb blockade."[37] $P(\varepsilon)$ was determined from equilibrium measurements at high magnetic field, where superconductivity is completely suppressed. Details of the fitting procedure used to extract $P(\varepsilon)$ were reported earlier.[12]

Quantitative analysis of our tunneling data requires an accurate determination of the superconducting gap Δ hence we fabricated a second S/I/N Tunnel junction simultaneously with the sample, but placed about 20 μm away from it, and with the N side of the junction far from any superconductor. Tunneling spectroscopy measurements on this reference junction, shown in Fig. 11(a), were fit to Eq. (10) with n_{Ag} independent of energy and with the standard BCS form for n_{Al}, to provide an accurate determination of Δ.

Several of our tunnel junctions exhibited sharp anomalies in the conductance data for voltages close to the superconducting gap; however, these features disappeared with the application of a small magnetic field of $B=12.5$ mT.[38] Figure 12 shows dI/dV data for one particular tunnel probe for different magnetic field strengths. Along with each data set are fits using the standard BCS form for $n_{\mathrm{Al}}(E)$ with a small depairing parameter proportional to B^2, which has been shown to account well for applied magnetic fields.[39] Adding this term effectively rounds the DOS in the superconductor. Following the notation of Ref. 39 we determined a depairing parameter of $\gamma \equiv \Gamma/\Delta=0.0020$ for $B=12.5$ mT and a superconducting gap in the Al of $\Delta=274$ μeV. This rather large

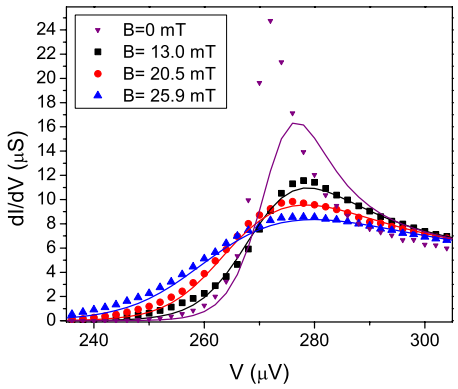

FIG. 12. (Color online) Expanded view of differential conductance data for eV near Δ from the tunnel probe far away from superconducting reservoirs, for select magnetic fields. Symbols represent data while solid lines are best fits to BCS theory using a single value of the gap Δ and a depairing strength proportional to B^2. Notice that the data at $B=0$ deviate significantly from the theory, whereas the data sets with $B>13$ mT are fit well by the theory.

value for Δ was consistent across samples and is believed to be due to oxygen incorporated into thin, thermally evaporated Al films.[40,41]

With the form for $n_{\mathrm{Al}}(E)$ confirmed, it is possible to analyze the dI/dV data for the sample tunnel probe, which is in close proximity to superconducting reservoirs. Figure 11(b) shows the dI/dV for this probe with an external field of 12.5 mT applied. The differences between the dI/dV data from tunnel probes nearby or far away from superconducting reservoirs arise from changes in the DOS of the normal wire due to the proximity effect. Rather than a flat DOS used to fit the data in Fig. 11(a), the DOS in the Ag wire near the superconducting reservoirs is modified as shown by the squares in Fig. 11(d). This shape was obtained by deconvolving the dI/dV data.

Also shown in Fig. 11(d) is the density of states of the Ag wire determined from a numerical calculation of the Usadel equation (solid line). This calculation requires knowledge of the sample dimensions, the gap in the superconducting reservoirs, and the Thouless energy. The sample dimensions were obtained from scanning electron micrographs, such as the one shown in Fig. 1. The gap in the superconducting reservoirs was found to be $\Delta \approx 150$ μeV. This value of Δ is much smaller than the value in the Al tunnel probe because the reservoirs are much thicker than the tunnel probes (and presumably contain much less oxygen), and because they are close to a normal metal-superconductor bilayer. Finally, the Thouless energy was determined by fitting the critical current vs temperature data as discussed in Sec. IV C. The value of E_{Th} was then refined through self-consistent calculations involving both the finite probe size and the position dependent order parameter Δ in the superconducting reservoirs.

When supercurrent flows through the S/N/S junction, the phase difference of the reservoirs ϕ changes $n_{\mathrm{Ag}}(E)$. For this reason, dI/dV data were also taken with supercurrent flowing across the S/N/S junction. The resulting fits of n_{Ag} for $I=0.9I_c$ and $I=-0.9I_c$, which are identical to each other, are

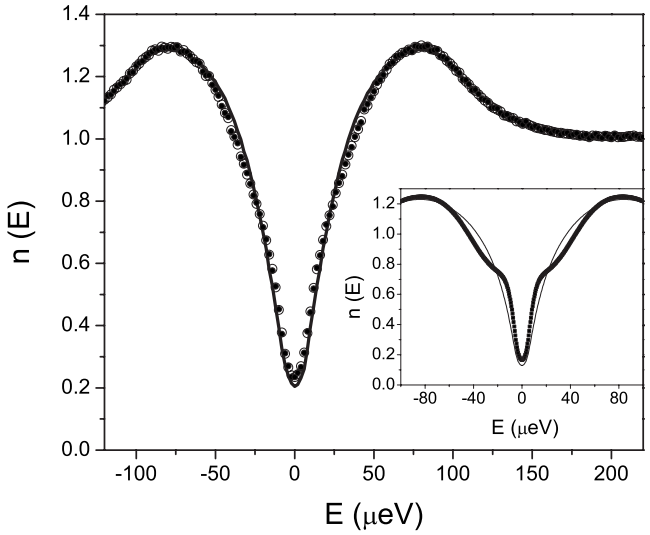

FIG. 13. (a) Density of states of Ag wire at location of tunnel probe with different amounts of supercurrent flowing across the S/N/S junction. Solid and hollow circles represent n_{Ag} for $I_s=0.9I_c$ and $I_s=-0.9I_c$, respectively, while the solid line is for $I_s=0$. Inset: Theoretical results of injecting supercurrent into device. Solid line for $I_s=0$ and dots for $I_s=\pm.9I_c$

shown in Fig. 13 along with one for $I=0$. It is noteworthy that the change of shape (more narrow at low energies, broader at intermediate ones) is qualitatively consistent with theoretical calculations shown in the inset.

It was anticipated that applying a voltage to the normal lead would not alter $n_{\mathrm{Ag}}(E)$ so that it would be possible to deconvolve the distribution function $f_{\mathrm{Ag}}(E)$ for the system out of equilibrium. Figure 14 shows that this assumption does not hold, as the best fits for applied voltages $U=22$ μV and $U=63$ μV are poor. Only by using an altered $n_{\mathrm{Ag}}(E)$ was it possible to fit the data in Fig. 14.

Changes in $n_{\mathrm{Ag}}(E)$ with increasing U are probably due to a slight suppression of the gap in the superconducting electrodes, which are adjacent to superconductor/normal-metal bilayers. To estimate how $n_{\mathrm{Ag}}(E)$ changes, we used two different forms for the distribution function $f_{\mathrm{Ag}}(E)$. First, we computed $f_{\mathrm{Ag}}(E)$ from Eqs. (9a) and (9b), which include

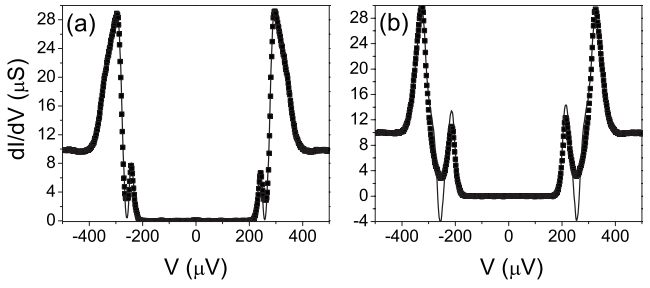

FIG. 14. Differential conductance tunneling data taken with a voltage U applied between N to S_1 to drive the system out of equilibrium. Solid lines are the best fits using the n_{Ag} data from Fig. 13. (a) $U=22$ μV. (b) $U=63$ μV. The fits are unable to reproduce the data.

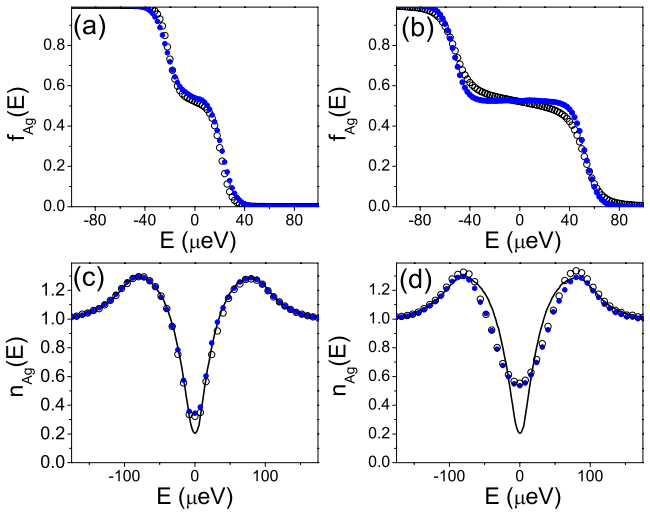

FIG. 15. (Color online) Calculated DOS using expected forms for distribution functions. (a) Distribution functions for $U=25$ μV. Solid circles were calculated by solving Eqs. (9) without collision integrals. Open circles were calculated by solving Boltzmann equation including collisions, but not including superconducting correlations. (b) Distribution functions for $U=63$ μV. Below are the deconvolved forms for n_{Ag} using the above distribution functions when (c) $U=25$ μV and (d) $U=63$ μV. In both, solid lines represent $U=0$ μV, for comparison.

proximity effects due to the nearby superconducting reservoirs, but neglect inelastic scattering. Second, we solved the diffusive Boltzmann equation with collision integrals for electron-electron scattering, while neglecting superconducting correlations. The two forms for the distribution functions are shown in Figs. 15(a) and 15(b) for two different values of U: 25 μV and 63 μV. Using those distribution functions, new densities of states were obtained by deconvolution of the dI/dV data and are shown as the symbols in Figs. 15(c) and 15(d). Notice that the two different forms of the distribution function yield similar results for n_{Ag}. Figures 15(c) and 15(d) also show n_{Ag} obtained from equilibrium dI/dV data, as the solid lines. However, the resulting n_{Ag} does not obey the sum rule

$$\int dE(n_{\mathrm{Ag}}-1)=0,$$

that should be valid in all situations. We do not know what causes this discrepancy.

Fortunately it is possible to extract information about $f_{\mathrm{Ag}}(E)$ using a method that is relatively insensitive to the exact form of $n_{\mathrm{Ag}}(E)$, by taking advantage of a near symmetry of the data with respect to the direction of I_S. The data shown in Fig. 13 confirm our expectation that $n_{\mathrm{Ag}}(E,U=0,I_S)=n_{\mathrm{Ag}}(E,U=0,-I_S)$, a symmetry that also holds approximately for $U\neq 0$. Hence, one can analyze the difference between two data sets with opposite directions of the supercurrent $dI/dV(V,U,I_S)-dI/dV(V,U,-I_S)$, which will depend on the differences in the distribution functions $\delta f_{\mathrm{Ag}}(E)\equiv f_{\mathrm{Ag}}(E,U,I_S)-f_{\mathrm{Ag}}(E,U,-I_S)$. The effect of analyz-

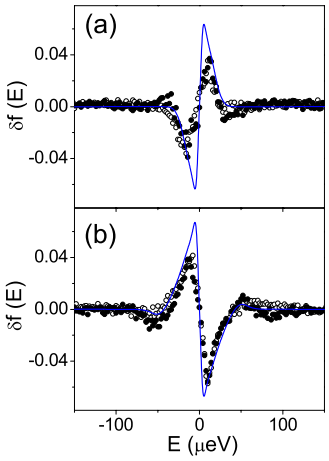

FIG. 16. (Color online) (a) $\delta f(E) \equiv f_{\mathrm{Ag}}(E,U,I_S) - f_{\mathrm{Ag}}(E,U,-I_S)$ for $U=22\ \mu$V and $I_S=0.9I_c$. (b) Same quantity for $U=63\ \mu$V and $I_S=0.9I_c$, where $U>34\ \mu$V corresponds to the system being in the π state. In both figures, a second data set (open circles) is shown with the signs of both U_N and I_S reversed. Solid lines are numerical solutions to Eq. (9).

ing the data with the wrong DOS for the Ag is greatly reduced in this case. The feature we seek in $\delta f_{\mathrm{Ag}}(E)$ is predicted to be odd in I_s, hence it should be the only contribution to $\delta f_{\mathrm{Ag}}(E)$. Figure 16(a) shows δf with $U=22\ \mu$V and $I_S=0.9I_c$, which exhibits the predicted feature that is antisymmetric in energy. The solid lines are the numerical solution to Eqs. (9), with the parameters E_{Th} and Δ obtained from the previous fits, with no additional fit parameters. The computed theory curves agree well with the experimental data.

A further test of the robustness of the experimental results is to compare the measured form of $\delta f_{\mathrm{Ag}}(E)$ when the signs of both U and I_S are reversed, i.e., $f_{\mathrm{Ag}}(E,-U,-I_S) - f_{\mathrm{Ag}}(E,-U,I_S)$. The results of this second measurement are shown superimposed on the first in Fig. 16(a). The agreement between the two data sets is excellent.

Interestingly, applying a voltage $U>34\ \mu$V brings this sample into its π state. Figure 16(b) shows $\delta f(E)$ data for $U=63\ \mu$V and $I_S=0.9I_c$. Compared to Fig. 16(a), the sign of the low-energy feature in $\delta f(E)$ is reversed, demonstrating that the phase difference ϕ, rather than the supercurrent, determines the sign of the new feature in $f(E)$.

The results of Fig. 16 indicate that the supercurrent has a large effect on the electron energy distribution function inside the normal metal. Such a mechanism has been utilized to explain[36] the large thermopower measured in Andreev interferometers[42]—systems with two normal-metal and two superconducting contacts. Our results confirm this mechanism and point out to new phenomena dependent on it, such as the large Peltier effect:[35] in linear response to the quasiparticle current (voltage), the supercurrent-induced change δf translates into a change of the electron temperature and the sign of this change (heating or cooling) depends on the relative sign of the supercurrent compared to the sign of the quasiparticle current. One can hence cool part of the structure by simultaneously applying a quasiparticle current and a supercurrent.

VII. CONCLUSIONS

Superconductor/normal-metal hybrid systems exhibit a wealth of fascinating behaviors, starting with the proximity and Josephson effects. Driven out of equilibrium, the possibilities increase, from the nonequilibrium π junction to the supercurrent-induced modification of $f(E)$ discussed in the final section of this paper. All of these observations can be interpreted with two main concepts: the spectrum of the supercurrent $j_E(E)$ and the electron distribution function $f(E)$. The latter can be tuned by applying voltages or changing the temperature—the previous for example by applying a magnetic field. In Secs. III, IV, and VI we showed in different schemes how the nonequilibrium $f(E)$ changes the observed supercurrent and how the supercurrent affects $f(E)$. In Sec. V we discuss the modifications in $j_E(E)$ due to a magnetic field and the resulting changes in the supercurrent. To our knowledge, the effect of a parallel magnetic field on the S/N/S critical current had not been explored in detail before.

As discussed in Refs. 9 and 10, the Zeeman effect due to a magnetic field will cause analogous changes in the supercurrent as the nonequilibrium population of the supercurrent carrying states. This exact analogy is distorted on one hand due to the inelastic scattering changing the nonequilibrium distribution function and, on the other hand, the orbital effect arising from the magnetic field. It remains an experimental challenge to show this analogy and combine the two effects in the case when the Zeeman effect dominates over the orbital effect. As we discuss in Sec. V, the latter would require constructing extremely thin junctions.

Recently there has been intense interest in the limit where a Josephson junction behaves as a coherent quantum system with one degree of freedom.[43] There is hope that Josephson junctions will someday provide the building blocks for a quantum computer. In the meantime, we hope to have demonstrated that even in the classical regime, the Josephson junction is full of surprising new possibilities. While preparing this manuscript, we learned about recent related works[31] where the magnetic field dependence of the S/N/S supercurrent was also studied.

ACKNOWLEDGMENTS

We thank H. Pothier, D. Esteve, and S. Yip for many valuable discussions. This work was supported by NSF Grants No. DMR-0104178 and 0405238, by the Keck Microfabrication Facility supported by NSF Grant No. DMR-9809688, and by the Academy of Finland.

APPENDIX A: USADEL EQUATION AND THE MAGNETIC FIELD

The Usadel equation in a magnetic field can be written as follows, making use of the θ parametrization $G=\cosh\theta$, $F=e^{i\chi}\sinh\theta$ of the quasiclassical Green's functions[4,6,9,10]

$$\hbar D\nabla^2\theta = -2i(E+\sigma h)\sinh\theta + \left(\hbar\Gamma_{\mathrm{sf}} + \frac{v_s^2}{2D}\right)\sinh 2\theta, \tag{A1}$$

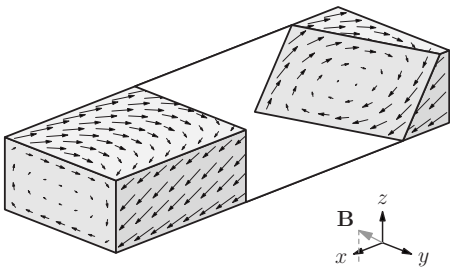

FIG. 17. Supercurrent flow induced by a magnetic field $\mathbf{B}=(B_x,B_y,B_z)\propto(3,1,2)$ in a thin rectangular wire. The arrows indicate the magnitude and direction of the superfluid velocity v_S. Fourth-order variational solution for χ is used here, see text.

$$\nabla(v_s \sinh^2\theta)=0, \quad v_s \equiv D[\nabla\chi - 2e\mathbf{A}/\hbar]. \tag{A2}$$

Here, D is the diffusion constant, $\mathbf{A}$ the vector potential, $\Gamma_{\rm sf}$ the spin-flip rate, v_s the gauge-invariant superfluid velocity, and $h=\frac{1}{2}g\mu|\mathbf{B}|$ the Zeeman energy. The equation is to be solved separately for both spin configurations $\sigma=\pm$, assuming spin-independent material parameters. The spin-averaged spectral supercurrent $j_E=\frac{1}{2}\,\mathrm{Im}[v_s \sinh^2\theta|_{\sigma=+} + v_s \sinh^2\theta|_{\sigma=-}]/D$ is obtained from the solutions and can be used to calculate the observable supercurrent under various conditions. Below, we consider these equations in a wire that has an uniform cross section S, and assume the boundary conditions

$$\chi = \pm\phi/2, \quad \theta=\theta_0, \quad \text{at } x=0,L, \tag{A3}$$

$$\hat{n}\cdot v_s = 0, \quad \hat{n}\cdot\nabla\theta = 0, \quad \text{on } \partial S, \tag{A4}$$

where ∂S is the boundary of S. These imply that we neglect details of the current distribution near the terminal-wire contact.

When a magnetic field is applied to a wire, in addition to the Zeeman splitting, the field induces circulating components to the supercurrent flowing in the wire (see Fig. 17). These currents contribute to decoherence, for example, reducing the magnitude of the critical current, and in the general case also prevent reducing Eqs. (A1) to one-dimensional equations in the direction parallel to the wire. For thin wires, however, the additional decoherence can be simply absorbed to the spin-flip parameter $\Gamma_{\rm sf}$ in the one-dimensional Usadel equation and the vector potential can otherwise be neglected.[33,39,44,45] Below, we show how this conclusion can be reached for an arbitrary orientation of the magnetic field, and that the results are consistent with the discussion in Sec. V.

Reducing Eq. (A1) to a one-dimensional equation is possible when the transverse dimensions d of the wire satisfy $d\ll L,l_m$, where L is the distance between the superconducting contacts and $l_m=\sqrt{\hbar/eB}$ a magnetic length scale. This is because θ varies on the length scales of l_m and $l_E=\sqrt{\hbar D/E}\sim L$ when considering energies $E\sim\hbar D/L^2$ relevant for the supercurrent. For perpendicular fields it is also possible to directly choose a proper London gauge where χ varies slowly in the transverse direction and $v_S\propto\mathbf{A}$.

Since $l_m\sim 80$nm for $B\sim 0.1$ T, in the experimentally interesting situation we have $w\lesssim l_m\ll l_E\sim L$. To handle the details of the problem in this case, we apply perturbation theory in the parameter $\lambda=d/L$. We choose a coordinate system such that x is the coordinate parallel to the wire and y and z correspond to transverse directions, and fix a convenient gauge $\mathbf{A}=(B_y z-B_z y,-B_x z,0)$ in which the vector potential is independent of x. Finally, we rewrite Eqs. (A1) in the dimensionless variables $\tilde{x}=x/L$, $\tilde{y}=y/\lambda L$, $\tilde{z}=z/\lambda L$, $\tilde{\mathbf{B}}=eL^2\mathbf{B}/\hbar\lambda$ and substitute in the regular series expansion $\theta=\theta_0+\lambda\theta_1+\lambda^2\theta_2+\cdots$, $\chi=\chi_0+\lambda\chi_1+\lambda^2\chi_2+\cdots$.

Requiring the equations corresponding to orders λ^{-2}, λ^{-1} and λ^0 of expansion to be separately satisfied, we first find that the variables θ_0, θ_1 and χ_0 are independent of y and z. We also find that the first-order response $\delta\chi=\lambda\chi_1$ is given by

$$\nabla_\perp^2\delta\chi=0, \quad \hat{n}\cdot\nabla_\perp\delta\chi|_{\partial S}=\hat{n}\cdot 2e\mathbf{A}/\hbar. \tag{A5}$$

Here, ∂S is the boundary of the cross-section of the wire, $\hat{n}$ its outward normal vector, and the operator $\nabla_\perp$ consists of the transverse components of the gradient. This x-independent result applies in the central parts of the wire, away from boundary layers near the ends of the wire. Finally, after averaging the equations of order λ^0 across the cross section S of the wire, we arrive at the result

$$\partial_x^2\theta_0 = -2i(E+\sigma h)\sinh\theta_0 + (\hbar\Gamma_{\rm sf}+\gamma)\sinh 2\theta_0, \tag{A6}$$

$$\partial_x(\sinh^2\theta_0\partial_x\chi_0)=0, \tag{A7}$$

$$\gamma \equiv \frac{\hbar D}{2S}\int_S dydz(\hat{x}\partial_x\chi_0+\nabla_\perp\delta\chi-2e\mathbf{A}/\hbar)^2. \tag{A8}$$

This shows how the effective spin-flip parameter is modified by the applied field $\mathbf{B}$.

The additional decoherence (A8) depends on the direction of the field and the cross section of the wire. For a wire with a circular cross section of radius R, we note that Eq. (A5) has the exact solution $\delta\chi=-eB_x yz/\hbar$. This results to

$$\gamma=\frac{1}{2}\hbar D(\partial_x\chi_0)^2+\frac{e^2D}{2\hbar}\left(\frac{1}{2}R^2B_x^2+R^2B_y^2+R^2B_z^2\right). \tag{A9}$$

For wires with a rectangular cross section, we cannot solve Eq. (A5) analytically. However, a variational solution is still possible: we can expand $\delta\chi$ in polynomials of y, z to orders $n\leq 3$ and project Eq. (A5) onto this function basis. From this procedure, we find

$$\delta\chi \approx -\frac{2eB_x}{\hbar}\frac{d_z^2}{d_y^2+d_z^2}yz, \tag{A10}$$

$$\gamma=\frac{1}{2}\hbar D(\partial_x\chi_0)^2+\frac{e^2D}{6\hbar}(\tilde{w}_{yz}^2B_x^2+d_z^2B_y^2+d_y^2B_z^2), \tag{A11}$$

$$\tilde{w}_{yz}^2\approx\frac{d_y^2d_z^2}{d_y^2+d_z^2}, \tag{A12}$$

where d_y and d_z are the width and thickness of the wire. For orders $n\leq 4$ we obtain instead

$$\tilde{w}_{yz}^2 = \frac{d_y^2 d_z^2}{d_y^2 + d_z^2}\left\{1 - \frac{266 d_y^2 d_z^2}{105 d_y^4 + 1500 d_y^2 d_z^2 + 105 d_z^4}\right\}. \quad \text{(A13)}$$

Approximations using higher-order basis produce only slight improvements in accuracy to γ.

We now note that the contribution of the magnetic field to the decoherence rate γ is of the form $e^2 D d^2 B^2/\hbar$ for all directions of the field, where d is proportional to some transverse dimension of the wire. Comparing this to the energy scale $E_T = \hbar D/L^2$ of the one-dimensional Usadel equation (A6), we find a dimensionless parameter $(eBLd/\hbar)^2 \propto (\Phi/\Phi_0)^2$ that determines how much the magnetic field suppresses coherence. Here, the flux Φ corresponds to an area $L \times d$, which is in agreement with the discussion in Sec. V.

Finally, note that above we neglected the screening of the magnetic field by the induced supercurrents. However, this should not be important in the experimental case, as the Josephson screening length $\lambda_J = \sqrt{\hbar d^2/2e\mu_0 I_c L} \gtrsim 200$ nm is larger than the width of the junction, and the aluminum terminals are sufficiently thin as to produce only small screening.

*Present address: Department of Physics, Taylor University, Upland, IN 46989, USA.

†Present address: Laboratoire de Photonique et de Nanostructures-CNRS, Route de Nozay, 91460 Marcoussis, France.

‡birge@pa.msu.edu

[1] P. G. de Gennes, Rev. Mod. Phys. **36**, 225 (1964).

[2] B. Pannetier and H. Courtois, J. Low Temp. Phys. **118**, 599 (2000).

[3] C. J. Lambert and R. Raimondi, J. Phys.: Condens. Matter **10**, 901 (1998).

[4] W. Belzig, F. K. Wilhelm, C. Bruder, G. Schön, and A. D. Zaikin, Superlattices Microstruct. **25**, 1251 (1999).

[5] J. J. A. Baselmans, A. F. Morpurgo, B. J. van Wees, and T. M. Klapwijk, Nature (London) **397**, 43 (1999).

[6] K. D. Usadel, Phys. Rev. Lett. **25**, 507 (1970).

[7] R. Shaikhaidarov, A. F. Volkov, H. Takayanagi, V. T. Petrashov, and P. Delsing, Phys. Rev. B **62**, R14649 (2000).

[8] J. Huang, F. Pierre, T. T. Heikkilä, F. K. Wilhelm, and N. O. Birge, Phys. Rev. B **66**, 020507(R) (2002).

[9] T. T. Heikkilä, F. K. Wilhelm, and G. Schön, Europhys. Lett. **51**, 434 (2000).

[10] S. K. Yip, Phys. Rev. B **62**, R6127 (2000).

[11] T. T. Heikkilä, T. Vänskä, and F. K. Wilhelm, Phys. Rev. B **67**, 100502(R) (2003). Note that in this reference there is a sign error in the $T(x)$ coefficient, which increases the amplitude of the change δf.

[12] M. S. Crosser, P. Virtanen, T. T. Heikkilä, and N. O. Birge, Phys. Rev. Lett. **96**, 167004 (2006).

[13] G. J. Dolan and J. H. Dunsmuir, Physica B **152**, 7 (1988).

[14] S. Gueron, Ph.D. thesis, University Paris VI, France, 1997.

[15] A. F. Volkov, Phys. Rev. Lett. **74**, 4730 (1995).

[16] A. F. Morpurgo, T. M. Klapwijk, and B. J. van Wees, Appl. Phys. Lett. **72**, 966 (1998).

[17] S. K. Yip, Phys. Rev. B **58**, 5803 (1998).

[18] F. K. Wilhelm, G. Schön, and A. D. Zaikin, Phys. Rev. Lett. **81**, 1682 (1998).

[19] I. O. Kulik, Sov. Phys. JETP **30**, 944 (1970).

[20] T. T. Heikkilä, J. Särkkä, and F. K. Wilhelm, Phys. Rev. B **66**, 184513 (2002).

[21] H. Pothier, S. Gueron, N. O. Birge, D. Esteve, and M. H. Devoret, Phys. Rev. Lett. **79**, 3490 (1997).

[22] B. J. van Wees, K.-M. H. Lenssen, and C. J. P. M. Harmans, Phys. Rev. B **44**, 470 (1991).

[23] J. J. A. Baselmans, T. T. Heikkilä, B. J. van Wees, and T. M. Klapwijk, Phys. Rev. Lett. **89**, 207002 (2002).

[24] V. T. Petrashov, V. N. Antonov, P. Delsing, and T. Claeson, Phys. Rev. Lett. **74**, 5268 (1995).

[25] A. F. Andreev, Sov. Phys. JETP **19**, 1228 (1964).

[26] F. Pierre, Ann. Phys. (Paris) **26**, 1 (2001).

[27] This procedure also neglects the (presumably weak) proximity effect on the kernel of the electron-electron collision integral. These are similar to those in bulk superconductors, see G. M. Eliashberg, Zh. Eksp. Teor. Fiz. **61**, 1254 (1971) [Sov. Phys. JETP **34**, 668 (1972)].

[28] K. E. Nagaev, Phys. Rev. B **52**, 4740 (1995).

[29] M. Henny, S. Oberholzer, C. Strunk, and C. Schonenberger, Phys. Rev. B **59**, 2871 (1999).

[30] M. S. Crosser, Ph.D. Thesis, Michigan State University, East Lansing, 2005.

[31] L. Angers, F. Chiodi, J. C. Cuevas, G. Montambaux, M. Ferrier, S. Guéron, and H. Bouchiat, e-print arXiv:0708.0205 (unpublished); J. C. Cuevas and F. S. Bergeret, Phys. Rev. Lett. **99**, 217002 (2007).

[32] V. V. Ryazanov, V. A. Oboznov, A. Yu. Rusanov, A. V. Veretennikov, A. A. Golubov, and J. Aarts, Phys. Rev. Lett. **86**, 2427 (2001).

[33] J. C. Hammer, J. C. Cuevas, F. S. Bergeret, and W. Belzig, Phys. Rev. B **76**, 064514 (2007).

[34] E. Scheer, H. v. Lohneysen, A. D. Mirlin, P. Wölfle, and H. Hein, Phys. Rev. Lett. **78**, 3362 (1997).

[35] P. Virtanen and T. T. Heikkilä, Phys. Rev. B **75**, 104517 (2007).

[36] P. Virtanen and T. T. Heikkilä, J. Low Temp. Phys. **136**, 401 (2004), and references therein.

[37] G. L. Ingold and Y. V. Nazarov, *Single Charge Tunneling Coulomb Blockade Phenomena in Nanostructures* (Plenum Press, London, 1992), Vol. 294.

[38] Similar behavior has been observed by other groups, cf. p. 40 of F. Pierre, Ann. Phys. (Paris) **26**, 1 (2001).

[39] A. Anthore, H. Pothier, and D. Esteve, Phys. Rev. Lett. **90**, 127001 (2003).

[40] R. B. Pettit and J. Silcox, Phys. Rev. B **13**, 2865 (1976).

[41] R. W. Cohen and B. Abeles, Phys. Rev. **168**, 444 (1968).

[42] J. Eom, C.-J. Chien, and V. Chandrasekhar, Phys. Rev. Lett. **81**, 437 (1998); A. Parsons, I. A. Sosnin, and V. T. Petrashov, Phys. Rev. B **67**, 140502(R) (2003).

[43] V. Bouchiat, D. Vion, P. Joyez, D. Esteve, and M. H. Devoret, Phys. Scr. **T76**, 165 (1998).

[44] W. Belzig, C. Bruder, and G. Schön, Phys. Rev. B **54**, 9443 (1996).

[45] P. G. deGennes, *Superconductivity of Metals and Alloys* (Perseus Books, Massachusetts, 1966), Chap. 8.